ORIGINAL ARTICLE

Salmonella-mediated blood−brain barrier penetration, tumor homing and tumor microenvironment regulation for enhanced chemo/bacterial glioma therapy

Ze Mi[a,†], Qing Yao[a,c,f,†], Yan Qi[c], Jinhai Zheng[e], Jiahao Liu[a], Zhenguo Liu[a], Hongpei Tan[a], Xiaoqian Ma[a], Wenhu Zhou[a,b,d,*], Pengfei Rong[a,d,*]

[a]Department of Radiology, The Third Xiangya Hospital, Central South University, Changsha 410013, China
[b]Xiangya School of Pharmaceutical Sciences, Central South University, Changsha 410013, China
[c]Department of Pathology, Shihezi University School of Medicine and the First Affiliated Hospital to Shihezi University School of Medicine, Shihezi 832003, China
[d]Key Laboratory of Biological Nanotechnology of National Health Commission, Changsha 410082, China
[e]School of Biomedical Sciences, Hunan University, Changsha 410082, China
[f]Department of Pathology, Cangzhou Central Hospital & the Affiliated to Hebei Medical University, Cangzhou 062650, China

Abstract Chemotherapy is an important adjuvant treatment of glioma, while the efficacy is far from satisfactory, due not only to the biological barriers of blood−brain barrier (BBB) and blood−tumor barrier (BTB) but also to the intrinsic resistance of glioma cells *via* multiple survival mechanisms such as up-regulation of P-glycoprotein (P-gp). To address these limitations, we report a bacteria-based drug delivery strategy for BBB/BTB transportation, glioma targeting, and chemo-sensitization. Bacteria selectively colonized into hypoxic tumor region and modulated tumor microenvironment, including macrophages repolarization and neutrophils infiltration. Specifically, tumor migration of neutrophils was employed as hitchhiking delivery of doxorubicin (DOX)-loaded bacterial outer membrane vesicles (OMVs/ DOX). By virtue of the surface pathogen-associated molecular patterns derived from native bacteria, OMVs/DOX could be selectively recognized by neutrophils, thus facilitating glioma targeted delivery

of drug with significantly enhanced tumor accumulation by 18-fold as compared to the classical passive targeting effect. Moreover, the P-gp expression on tumor cells was silenced by bacteria type III secretion effector to sensitize the efficacy of DOX, resulting in complete tumor eradication with 100% survival of all treated mice. In addition, the colonized bacteria were finally cleared by anti-bacterial activity of DOX to minimize the potential infection risk, and cardiotoxicity of DOX was also avoided, achieving excellent compatibility. This work provides an efficient trans-BBB/BTB drug delivery strategy *via* cell hitchhiking for enhanced glioma therapy.

1. Introduction

Glioma is the most common form of brain tumor, which is characterized by poor prognosis, short lifetime, and high mortality[1,2]. Chemotherapy is one of the main clinical methods to combat glioma. However, the current treatment efficacy is severely limited by both biological barriers of brain and multiple drug resistances of glioma cells. For example, the blood−brain barrier (BBB) and blood−tumor barrier (BTB) restrict the entrance of the vast majority of drugs into tumor tissue[3−5]. Even after being delivered inside cells, the cunning tumor cells could still pump out the drugs *via* up-regulation of P-glycoprotein (P-gp), leading to treatment failure[6]. To this end, extensive efforts have been made to the design of multi-functional nanomedicines with multiple surface modification[7−11], which could not only enhance the BBB/BTB transportation and deep tumor penetration but also reverse drug resistance[12−17]. While diverse nanoparticles have been developed with high drug loading, versatile surface modifications and smart drug release, tumor targeting efficiency and therapeutic outcomes still remain unsatisfactory for most of them[18,19]. One critical reason is that, compared to other types of tumors, the enhanced permeability and retention (EPR) effect in glioma is rather poor for nanoparticles due to the compact anatomical structures of brain tissue[20,21]. Although several active targeting strategies have also been attempted to simultaneously bypass BBB/BTB and target tumor tissue for improved anti-glioma efficacy, the *in vivo* performance is still suboptimal because of the negative effect of protein corona[22−24]. Therefore, next generation of drug delivery systems is deemed necessary for targeted glioma therapy.

Besides nanoparticle optimization, great research interest has been attracted on the employment of biochemotactic effect to realize tumor-targeted delivery, which is considered to be much more efficient[25,26]. For example, the early stage of tumor is featured with an inflammatory microenvironment, which recruits a large number of immune cells homing to tumor tissue through a process known as chemotaxis[27,28]. The migration of these immune cells can be adapted as hitchhiking delivery strategy to facilitate tumor-targeted delivery, among which neutrophils as the most abundant subtype have been widely used by virtue of the capability to penetrate inflamed tissues[29−33]. However, with the progression of tumor, the established tumor microenvironment instead is converted to immune-suppressive microenvironment, which attenuates such biochemotactic effect[34,35]. To reinforce this, various attempts have made to enhance the inflammation in tumor tissue by external photodynamic and photothermal therapies[36−39], while the limited tissue penetration of the light strongly restricts their clinical applications. Notably, the neutrophils have also been

exploited as vehicles to deliver anti-cancer drugs into glioma attributable to intrinsic activity of neutrophils to cross BBB/BTB and penetrate into glioma tissue[40]. However, surgical intervention was required to induce an inflammation reaction in the brain, which cannot be generalized applied to all glioma patients. Moreover, such a delivery system was prepared by assembling nanoparticles into neutrophils *ex vivo*, which is rather difficult to realize industrialization due to the complicated process of neutrophil isolation, short lifetime of neutrophils (only a few hours), premature intracellular degradation, as well as the risk of in vitro contamination. Therefore, alternative methods that can hitchhike neutrophils *in situ* during blood circulation are needed for real-world applications. Nevertheless, there is a still lack of mild and generalizable method to trigger glioma inflammation for neutrophil-mediated hitchhiking drug delivery.

Recently, we reported the used of anaerobic bacteria of *Salmonella* as a "Trojan horse" to enable tumor homing of nanoparticles by virtue of the selective colonization and growth of *Salmonella* in hypoxic region of tumor[41]. Owing to the facultative anaerobic nature, *Salmonella* could achieve more than 1000-fold accumulation in tumor tissue than in normal organs[42], and exert anti-tumor effect *via* various mechanisms for bacteria-mediated tumor therapy, such as inducing tumor cell apoptosis and autophagy, and regulating tumor immune microenvironment[43−45]. Interestingly, we found that, in addition to damaging tumors, *Salmonella* could also trigger significant infiltration of neutrophils into tumor[41]. While the neutrophil migration might compromise the therapeutic efficacy of the bacteria by eliminating bacteria or restricting the bacteria within the central necrotic areas of tumor[46,47], such unwanted effect might also be transformed into an advantage of neutrophil-mediated hitchhiking drug delivery.

Herein, we proposed a bacteria-based drug delivery strategy *via* hitchhiking circulating neutrophils (Scheme 1). The bacteria used in this work were engineered *Salmonella typhimurium* (*S.t*-ΔpG^FlaB) we reported previously[48], which are defective in guanosine 5′-diphosphate-3′-diphosphate synthesis (ΔppGpp *S. typhimurium*) and express therapeutic gene of *Vibrio vulnificus* flagellin B (FlaB). The excretion of FlaB not only re-educated macrophage for M2-to-M1 repolarization, but also promoted the recruitment of neutrophils[48−50]. To hitchhike the neutrophils *in vivo*, the doxorubicin (DOX) was facilely loaded into outer membrane vesicles of *S.t*-ΔpG^FlaB (forming OMVs/DOX). This design was inspired by the natural functions of neutrophils to fight invading pathogens through selective recognition of pathogen-associated molecular patterns (PAMPs)[51−53]. Because of heritage of PAMPs from the native bacteria, OMVs/DOX were
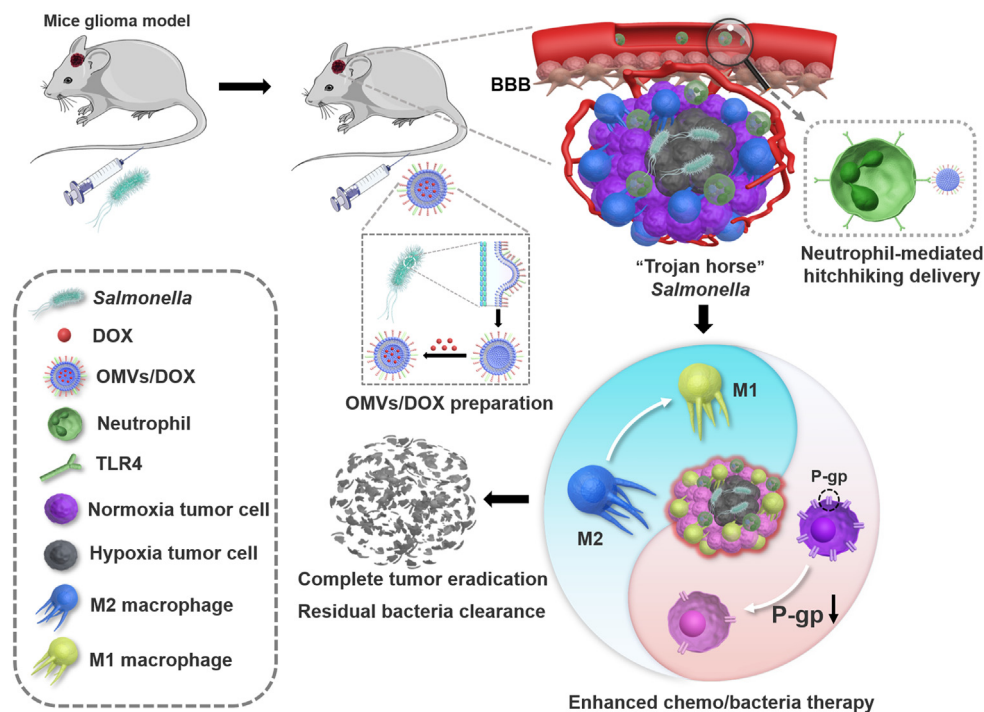
Scheme 1 Schematic illustration showing the bacteria-based drug delivery system to enable tumor homing delivery and enhanced anti-glioma therapy. The injection of bacteria could selectively colonize into hypoxic glioma tumor tissue to exert triple functionalities: repolarizing M2 macrophages into M1 phenotype, down-regulating P-gp protein on glioma cells, and most importantly, recruiting neutrophils. The DOX was loaded into the bacterial outer membrane vesicles (OMVs), which can be captured and engulfed *in vivo* by neutrophils by recognizing the PAMPs with toll-like receptor 4 (TLR4). Through hitchhiking neutrophils, the OMVs/DOX could effectively transport blood−brain barrier (BBB) and accumulate into tumor. The enhanced chem/bacterial therapy achieved complete tumor eradication with high compatibility.

effectively recognized and phagocytized by neutrophils, thus hitchhiking circulating neutrophils for subsequent BBB/BTB penetration and tumor-targeted delivery[54,55]. Through the bio-chemotaxis of bacteria, the tumor accumulation of drug was markedly enhanced by 18-fold as compared to OMVs/DOX delivered solely by passive targeting effect. Strikingly, $S.t$-ΔpG^{FlaB} could silence the expression of P-gp *via* type III secretion effector of SipA to sensitize the anti-tumor effect of DOX, achieving complete tumor eradication and 100% survival of all treated mice. Moreover, the potential bacterial infection risk has been minimized by antibacterial activity of DOX, and the cardiotoxicity of DOX was also reduced due to targeted drug delivery. Taken together, this bacteria-based cell hitchhiking strategy holds great potential for targeted and enhanced glioma therapy.

2. Materials and methods

2.1. Materials

Dulbecco's modified Eagle's medium (DMEM), fetal bovine serum (FBS) and penicillin-streptomycin solution were purchased from Gibco Life Technologies, Inc. (Grand Island, NY, USA). Paraformaldehyde was purchased from Biosharp (Hefei, China). 4′,6-Diamidino-2-phenylindole (DAPI) and LB broth were purchased from Solarbio Biotech Co., Ltd. (Beijing, China), and 3-(4,5-dimethylthiazol-2-yl)-2,5-diphenyl tetra zolium bromide (MTT) was from Sigma−Aldrich Co., Ltd. (St.Louis, MO, USA). Doxorubicin hydrochloride was purchased from Luoen (China). Fluorescence labelled antibodies against CD45, CD11b, F4/80, CD206, Ly6G and CD86 were purchased from Abcam

(Cambridge, England). The murine monoclonal P-gp C219 and TLR4 Polyclonal antibody were purchased from Abcam (Cambridge, England). XenoLight D-Luciferin Potassium Salt were purchased from PerkinElmer (Waltham Mass, USA).

2.2. Tumor cell lines and bacteria

The C6 cell (rat glioma cells) line was cultured in DMEM containing 10% FBS and 1% penicillin-streptomycin in a 37 °C incubator with 5% CO_2. The RAW 264.7 (mouse macrophage cells) was cultured in 1640 containing 10% FBS and 1% penicillin-streptomycin in a 37 °C incubator with 5% CO_2. The primers, plasmids, and bacterial strains used in this study ($S.t$-ΔpG^{lux}/$S.t$-ΔpG^{FlaB}) were kindly provided by Shengnan Jian from Chonnam National University of Korea. The bacteria were grown in LB medium at 37 °C with shaking at 200 rpm.

2.3. Animals

Healthy female nude mice (6−8 weeks) were purchased from the Department of Laboratory Animals, Central South University (Changsha, China) and were housed in environmentally controlled conditions (22 °C, 12 h light/dark cycle) with *ad libitum* access to standard laboratory chow and water. The study protocol was approved by the local Institutional Ethics Review Committee and the animal study was carried out in accordance with the established ethical guidelines for animal use and care at Central South University. To create the brain tumor model, the mice were intracranially inoculated with 1×10^6 C6 cells suspended in PBS (5 μL).

2.4. Isolation, purification, and characterization of OMVs

The $S.t$-ΔpG were inoculated into sterilized LB and cultured overnight at 37 °C with shaking at 200 rpm. The culture medium was centrifuged (4 °C, 5000 rpm, Fresco21) for 10 min to obtain the supernatant, which was filtered using a 0.22 mm filter to remove maternal bacterial debris and other contaminants. The supernatant was then concentrated using 100 kDa ultrafiltration tubes (Millipore Amicon) and washed twice with phosphate buffered saline (PBS) to obtain crude OMVs. Purified OMVs were obtained by ultracentrifugation using density gradient centrifugation for 2 h (4 °C, 200,000×g), and stored at −80 °C. The concentration of OMVs was analyzed by BCA protein kit. The morphology and size of OMVs were observed by transmission electron microscopy (TEM) and dynamic light scattering (DLS), respectively.

2.5. Preparation and characterization of OMVs/DOX

DOX and OMVs were gently mixed in PBS at an appropriate mass ratio, followed by 4 h incubation at 37 °C. The unloaded DOX was removed by using a 100 kDa ultrafiltration tube (5000×g, 10 min), and the obtained OMVs/DOX was then washed several times with PBS. The concentration of entrapped DOX in OMVs was quantified by a fluorescent microplate reader (E_x/E_m 480/590 nm) after cracking the OMVs using methanol emulsion (adding 10 × volume of methanol for 30 min ultrasonication and then centrifugation at 10,000×g for 10 min). The drug loading efficiency (LE) and encapsulation efficiency (EE) of OMVs/DOX can be determined as following Eqs. (1) and (2):

$$EE\,(\%) = (\text{The mass of DOX encapsulated in OMVs})/(\text{Total mass of DOX used to prepare the OMVs}) \times 100 \qquad (1)$$

$$LE\,(\%) = (\text{The mass of DOX encapsulated in OMVs})/(\text{Total mass of OMVs}) \times 100 \qquad (2)$$

The zeta potential, particle size, and polydispersity index (PDI) of OMVs/DOX were measured by DLS, and the morphology was examined using TEM. To study the drug release profile, OMVs/DOX was added into a dialysis bag (MWCO:3500) for dialysis under various PBS buffers. At predetermined timepoints, 1 mL sample was collected and replaced with 1 mL fresh PBS. The DOX concentration in the release medium was quantified using a fluorescent microplate reader at E_x/E_m 480/590 nm.

2.6. Cellular uptake of OMVs/DOX in vitro

A density gradient centrifugation method was employed to isolate neutrophils from peripheral blood in the orbital venous plexus of mice. Neutrophils or HBMEC cells (1.0 × 10^5 per dish) were seeded in confocal dishes and incubated with DOX or OMVs/DOX for 1 h, followed by washing three times with PBS. Cells were fixed with 4% paraformaldehyde for 20 min, and the nuclei were stained with DAPI (1 μg/mL) for 10 min, followed by visualization using a confocal laser scanning microscopy (CLSM). For flow cytometry (FCM) quantification, the cells (2.0 × 10^5 per well) were placed into a 6-well plate and incubated with DOX or OMVs/DOX for 1 h, and then the cells were collected into a centrifuge tube and washed twice with PBS, followed by adding 0.5 mL PBS for FCM.

2.7. Cytotoxicity assay

C6 cells (5 × 10^3 cells per well) were seeded into a 96 well plate and incubated overnight. After washing twice with PBS, different concentrations of drugs were added for another 24 h incubation. Then, the cells were treated with 100 μL MTT solution (0.5 mg/mL) for 4 h. After removing the medium, 100 μL DMSO was added to dissolve the formazan crystals. The absorbance at 490 nm was measured by a microplate reader (Inf nite M200 PRO, TECAN, Austria).

2.8. Bactericidal effect

$S.t$-ΔpG was grown at 37 °C to the mid-logarithmic phase in LB broth, and then diluted to a concentration of 2 × 10^4 colony forming units (CFU)/mL with sterile saline. Then, different concentrations of DOX or OMVs/DOX was added. Afterwards, the sample was dotted onto solid LB agar plates and cultured at 37 °C for 24 h, followed by counting the colonies on the plates to calculate the inhibition rate.

2.9. In vitro macrophage repolarization induced by $S.t$-ΔpG^{FlaB}

The macrophage repolarization effect of $S.t$-ΔpG^{FlaB} was investigated by flow cytometry and Western blot. For flow cytometry, RAW 264.7 cells (2 × 10^5 cell/well) were seeded into 6 well plates and stimulated with IL-4 (100 ng/mL) for 24 h to allow M2 polarization. After being treated with $S.t$-ΔpG^{FlaB} (the bacteria were pre-stimulated with 0.2% L-arabinose) for 48 h, the cells were collected, washed with PBS several times, and then resuspended in PBS. FITC labeled anti-CD80 or CD206 antibodies were added and incubated at 4 °C for 1 h. Finally, the fluorescence intensity was detected by flow cytometry (facsverse, BD, USA). For Western blot analysis, the cells were received the same treatments as above. Then, total proteins were extracted with RIPA lysate and quantified by BCA protein assay kit. Samples of equal amounts of protein were separated on sodium dodecyl sulfate polyacrylamide gel electrophoresis (SDS-PAGE) and then transferred to PVDF membranes. Membranes were blocked with 5% fetal bovine serum (FBS) and then incubated overnight at 4 °C with primary antibodies against CD80, CD206, and β-actin. After further incubation with HRP conjugated secondary antibody for 2 h, the membrane was visualized by ECL.

2.10. P-gp expression analysis

C6 cells (2 × 10^5 cells/well) were incubated in 6-well plates overnight. Then, the PBS, $S.t$-ΔpG^{FlaB} as well as $S.t$-ΔpG^{FlaB} supernatants were added to well plates for 24 h incubation. After treatments, total proteins were extracted with RIPA lysate and quantified using a BCA protein assay kit. Samples of equal amounts of protein were separated on SDS-PAGE and then transferred to PVDF membranes. Then, the membranes were blocked with 5% fetal bovine serum (FBS) and then incubated overnight at 4 °C with anti-mouse P-gp monoclonal antibody and β-actin. After incubation with HRP conjugated secondary antibody for 1 h, the membrane was visualized by ECL.

2.11. Cytotoxicity effect of DOX on C6 cells

C6 cells (5000 cells/well) were incubated in 96-well plates overnight. Then, the cells were incubated with PBS, OMVs/DOX, $S.t$-

ΔpG^{sup}, DOX, *S.t*-ΔpG^{sup} + DOX, *S.t*-ΔpG^{sup} + OMVs/DOX for 24 h respectively. Then, the cells were treated with 100 μL CCK8 solution (0.5 mg/mL) for 2 h. The absorbance at 450 nm was measured by a microplate reader (Inf nite M200 PRO, TECAN, Austria).

2.12. Uptake of DOX by C6 cells

The C6 cells (4×10^4 cells/well) were seeded into confocal dishes and incubated overnight, treating with or without *S.t*-ΔpG^{FlaB} supernatant for 24 h. After removing the supernatant, the cells were washed with PBS twice, and then incubated with DMEM, DOX, or OMVs/DOX for 4 h. After various treatments, the cells were washed with PBS twice, and placed into the CLSM for observation.

2.13. Optical bioluminescence imaging of *S.t*-ΔpG^{lux} in vivo

Nude mice ($n = 5$) were intravenously injected with 0.2 mL of sterile saline containing 8×10^6 CFU of *S.t*-ΔpG^{lux}. After anesthetization of the mice with 4% chloral hydrate, bioluminescence imaging was performed with the IVIS 100 system (Caliper Life, Sciences, Hopkinton, MA, USA) at 0, 24, 48 and 72 h after *S.t*-ΔpG^{lux} injection.

2.14. Immunofluorescence for macrophage and neutrophil

Nude mice were intravenously injected with 0.2 mL of sterile saline containing 8×10^6 CFU of *S.t*-ΔpG^{FlaB}. Tumor tissues were harvested at 72 h after injection, followed by being embedded in paraffin and sliced. After deparaffinization and rehydration, the slices were incubated with primary antibodies against CD86, CD206, CD11b and Ly6G at 4 °C overnight, and then fluorescent-labeled secondary antibodies for 30 min. The slices were observed by CLSM after being counterstained with DAPI.

2.15. Flow cytometry

The proportion of neutrophils, M1 and M2 macrophages in the tumor tissues were investigated by flow cytometry analysis. Briefly, tumor tissues were dissociated into single cell suspensions. Then the cells were stained using fluorescence-labelled antibodies CD45, CD11b, Ly6G, F4/80, CD206 and CD86 according to the manufacturer's instructions. Samples were analyzed using BD LSR Fortessa analyzer (BD Biosciences). Data were analyzed by FlowJoInit.

2.16. Biodistribution of DOX

The mice were randomly divided into 4 groups ($n = 3$): (1) *S.t*-ΔpG + OMVs/DOX; (2) OMVs/DOX; (3) DOX; (4) *S.t*-ΔpG + DOX. Each group were intravenously injected with 0.2 mL of sterile saline containing 8×10^6 CFU of *S.t*-ΔpG. After two days, each mouse received an equivalent dose of DOX (2 mg/kg). After anesthetization of the mice with 4% chloral hydrate, excitation light imaging was performed with the IVIS 100 system (Caliper Life, Sciences, Hopkinton, MA, USA) at 8 h after DOX or OMVs/DOX injection.

2.17. In vivo antitumor efficacy

The mice were randomly divided into six groups as described in main text. The equivalent dose of *S.t*-ΔpG^{FlaB} and DOX was 8×10^6 CFU and 2 mg/kg, respectively. The body weights of the tumor-bearing mice were monitored every other day throughout the study. On Day 15 after the tumor cells injection, the tumor sizes were monitored using a 7.0T micro-MRI scanner (Bruker BioSpec, Germany). At the end of the experiment, the mice were euthanized, and the tumors were collected to calculate the volume by the following equation: (length $\times$ width^2)/2. Serum was collected to measure the levels of IL-6, CXCL10, TNF-α, IL-12, LPS by ELISA, and the expression levels of IL-6 and TNF-α in brain, liver, spleen and kidney were measured by ELISA.

2.18. Biodistribution of *S.t*-ΔpG^{FlaB} after treatment in vivo

The colony formation assays were performed to study the biodistribution of *S.t*-ΔpG^{FlaB} in vivo. The collected tissues of brain, liver, spleen and tumor were homogenized in sterile water and then diluted. The serially diluted homogenates were plated onto solid LB agar plates and cultured at 37 °C. After 24 h, the colonies on the plates were counted. The biodistribution of *S.t*-ΔpG^{FlaB} was calculated according to the following Eq. (3):

$$\text{Counting CFUs (CFU/g)} = \text{Bacteria count} \times \text{Dilution factor/Tissue weight} \tag{3}$$

2.19. Biochemical analysis

The myocardial enzyme spectrum, hepatic and renal function of mice were analyzed by blood biochemical analysis. On Day 15 after treatments, serum was collected to measure the levels of lactate dehydrogenase (LDH-L, LDH1), creatine kinase (CK), serum aspartate transaminase (AST), alanine transaminase (ALT), serum creatinine (Cr) and blood urea nitrogen (BUN), and the untreated mice were used as the control group.

2.20. Haematoxylin and eosin (H&E) staining

The collected the major organs including brain, heart, liver, spleen, lung and kidney were fixed with 4% paraformaldehyde for 24 h, and embedded in paraffin and sliced. Then, the sections were stained with H&E and the images were obtained by a light microscope.

2.21. Hemolysis rate assay

The suspension of RBCs was added with an equal volume of PBS, OMVs/DOX, *S.t*-ΔpG^{FlaB}, *S.t*-ΔpG^{FlaB} + DOX, *S.t*-ΔpG^{FlaB} + OMVs/DOX, and 1% tritox aqueous solution, respectively. After 3 h incubation, the sample was centrifuged (Fresco21) at 10,000 rpm for 5 min, and 100 μL of supernatant was collected to measure the absorbance at 540 nm with a microplate reader.

2.22. Statistical analysis

All results are presented as mean $\pm$ standard deviation. The two-tailed Student's *t*-test was used to compare the means of pairs of groups. Differences were regarded as statistically significant at *$P < 0.05$, **$P < 0.01$, ***$P < 0.001$. Data are presented as mean $\pm$ SD.

3. Results and discussion

3.1. Preparation and characterizations of OMVs/DOX

The OMVs were derived from *Salmonella* by multiple centrifugation and ultrafiltration, and then purified by density gradient ultracentrifugation. The obtained OMVs had an average diameter of 94 nm with narrow particle size distribution (PDI = 0.212) (Fig. 1A), and a negative surface charge of −9.72 mV (Fig. 1B). The OMVs showed a typical spherical morphology based on TEM observation (Fig. 1C), and the structure had the same protein profile as the original bacteria according to SDS-PAGE analysis (Fig. 1D). All these features were consistent with previous report[56], confirming the successful preparation of OMVs. Then, various concentrations of DOX were added into OMVs to allow drug loading, and the optimal loading capacity was achieved at DOX to OMVs weight ratio of 1:1 (Fig. 1E), reaching ∼25% DOX loading. Such loading capacity was markedly higher than many liposomal-based nanomedicine[57]. After DOX loading, the OMVs/DOX complex did not show an obvious morphology change (Supporting Information Fig. S1), while the surface became less negative owing to DOX adsorption. In addition, the DOX loading can be easily observed by virtue of intrinsic red fluorescence of DOX (E_x = 485 nm) (Fig. 1F). The drug exhibited a two-phase release profile at both physiological pH of 7.4 and acidic pH of 5.0 (Fig. 1G). Within initial 12 h, ∼40% of the drug was released, likely due to the detachment of surface adsorbed DOX, followed by a much slower phase. Overall, the OMVs/DOX displayed a sustained release profile, which is beneficial for prolonged *in vivo* circulation and targeted delivery into brain.

We then explored the bio-functions of the OMVs as drug delivery carrier. It is known that the bacteria-derived OMVs contain several key components of bacteria such as pathogen-associated molecular patterns (PAMPs), which can be recognized by neutrophils *via* Toll like receptors (*e.g.*, TLR4) for neutrophil-mediated delivery. To demonstrate this, we isolated the neutrophils from mouse and treated with OMVs/DOX. The neutrophils exhibited a lobulated nuclear characteristic (Fig. 1H). After incubation with OMVs/DOX, a bright red fluorescence of DOX was observed inside cells, indicating the drug internalization. Interestingly, the uptake of nanoparticles can be largely blocked by TLR4 antibody (anti-TLR4) as evidenced by a significant decrease of DOX signal, confirming the critical contribution of TLR4-mediated OMVs/DOX delivery. We further quantified the intensity by flow cytometry analysis, and the result was consistent with above observation (Supporting Information Fig. S2). As a control, we also incubated OMVs/DOX with human brain microvascular endothelial cells (HBMEC), while in this case only weak fluorescence was observed. Therefore, OMVs/DOX could be selectively internalized into neutrophils, which acted as "hitchhike" to facilitate drug delivery into bacteria colonized brain tumor. The free DOX, by contrast, showed strong fluorescence in both neutrophils and HBMEC cells and was not influenced by TLR4 antibody due to non-specific penetration of the DOX, which may cause unwanted side-effects.

Next, the pharmacological activities of DOX were explored. As an anti-tumor drug, a concentration-dependent inhibition of C6 glioma cells was observed for both free DOX and OMVs/DOX, based on which the IC_{50} values were calculated (Fig. 1I). Besides, we further explored the anti-bacteria effect of DOX, and the inhibition curves were also obtained (Fig. 1J). Overall, the anti-tumor and anti-bacteria activities of DOX were quite similar by virtue of the same mechanism, resulting in comparable IC_{50} values (Fig. 1K). Note that free DOX showed slightly higher activity than OMVs/DOX at cellular level because it can directly diffuse into cells and function without a release step. However, OMVs/DOX is advantageous for *in vivo* applications owing to its superior BBB penetration and tumor targeting activities (*vide infra*). After accumulation into tumor tissue, OMVs/DOX could not only exert the anti-tumor effect for tumor therapy, but also kill the colonized bacteria to avoid the potential risk of bacterial infection.

3.2. Tumor colonized *S.t-ΔpGFlaB* to facilitate tumor homing and tumor cell accumulation of OMVs/DOX

Having performed a systematic characterization of OMVs/DOX and demonstrated its capability to selectively internalize into "hitchhike" neutrophils, we next studied the functions of *Salmonella*. *Salmonella* used in this study was *S.t-ΔpG*^{FlaB}, a type of avirulent *S. typhimurium* strain with suppressed endotoxin gene expression *via* relA and SpoT double mutation to inhibit ppGpp synthesis[58]. Such bacterium was tagged with FlaB, which can overexpress and secrete heterologous bacterial flagellin (FlaB) upon ʟ-arabinose stimulation. The safety of such bacteria has been significantly improved after detoxification[59], which has entered clinical trial for tumor therapy[60]. From TEM, the *S.t-ΔpG*^{FlaB} showed a typical ellipsoid shape with length of 3 μm (Fig. 2A). To track the *in vivo* biodistribution, *S.t-ΔpG*^{FlaB} was further labeled with a luciferase gene, which was able to emit strong bioluminescence in LB agar upon excitation (Fig. 2B). We then intravenously injected the bacteria into mice, and observed at 48 h post-injection by an *in vivo* IVIS image system. Interestingly, a bright fluorescence was observed in brain tissue of orthotopic glioma mice model as compared to normal mice (Fig. 2C), indicating the tumor tropism. Such BBB penetration activity could be partially attributable to the outer membrane protein A (OmpA), which could interact with gp96 protein (also known as GRP94, which is expressed at the surface of BBB endothelial cells) to facilitate bacteria penetrating through the BBB[7]. We then performed a dynamic monitoring on glioma mouse model, in which a significant increase of fluorescence in the brain was seen over 48 h (Fig. 2D). We further collected the tumor tissue and quantified the fluorescence, in which the intensity rapidly enhanced in the first 48 h, followed by leveling-off (Fig. 2E). Therefore, the bacterial could successfully penetrate BBB and colonize into glioma tissue, which acted as "Trojan horse" to elicit a strong inflammation at tumor site[61,62].

As "Trojan horse", the most critical role of tumor colonized *S.t-ΔpG*^{FlaB} was to recruit neutrophils as "hitchhike" to facilitate the accumulation of OMVs/DOX into tumor. To demonstrate this, the infiltration of neutrophils in tumor was explored by fluorescent co-staining of CD11b/Ly6G, the specific biomarkers of neutrophils. The tumor tissue in brain can be localized by H&E staining with an obvious pathological change, and the DAPI staining of the cell nuclei further confirmed the abnormal proliferation of the tumor tissue (Fig. 2F). Without treatment, almost no fluorescence was observed in tumor tissue because of minimal neutrophil infiltration. With pre-treatment of *S.t-ΔpG*^{FlaB}, on the contrary, a strong CD11b/Ly6G co-localized signal was observed in the tumor tissue (producing merged orange fluorescence), attributable to the bacteria-mediated neutrophils infiltration. We further quantified the neutrophil infiltration, and the CD11b/Ly6G dual-positive fluorescence was enhanced by 8.6-fold after bacteria colonization, demonstrating the strong neutrophil recruitment
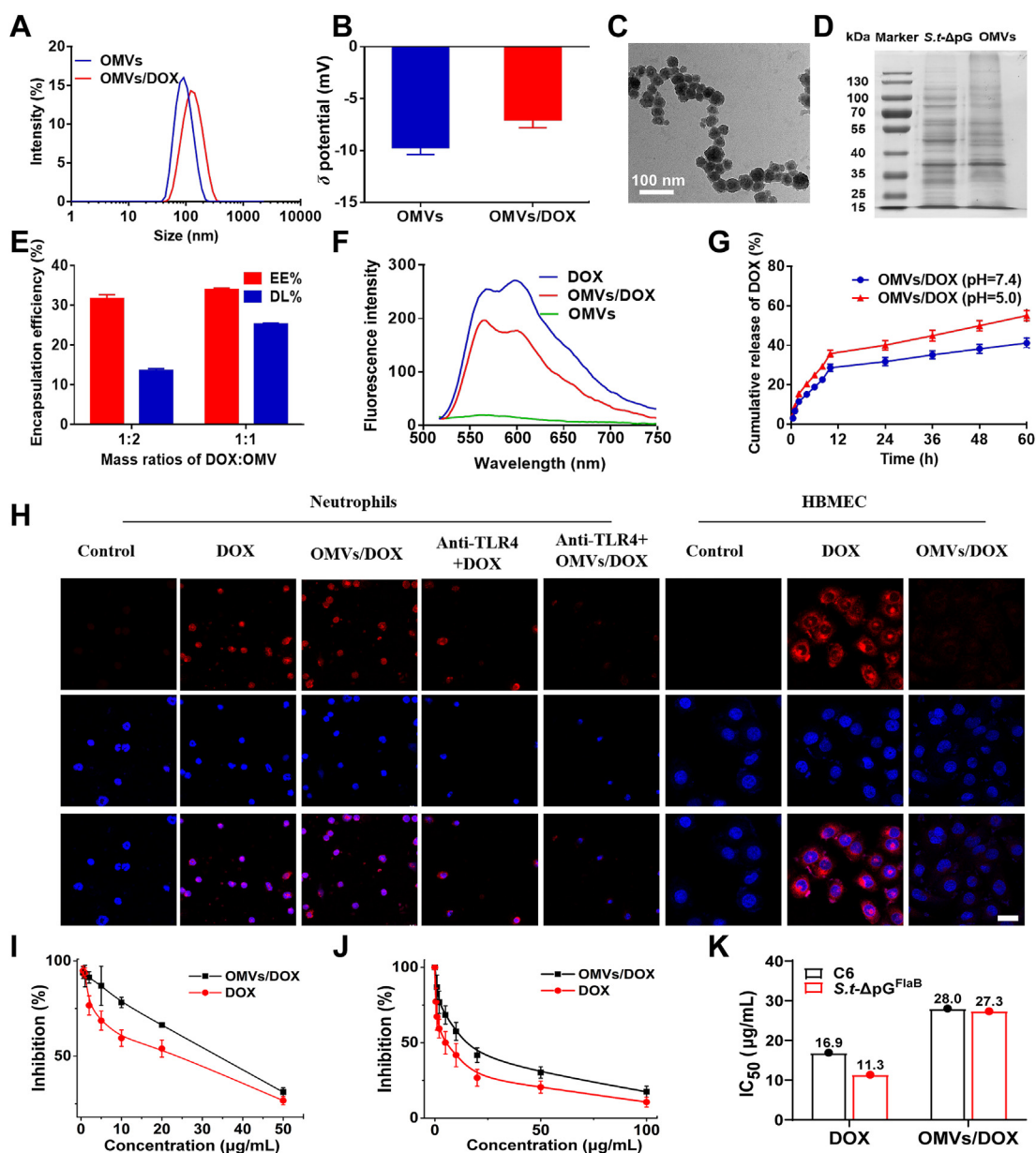
Figure 1 Characterization and bio-functions of OMVs/DOX. (A) The size distribution and (B) zeta potential of OMVs and OMVs/DOX DLS. $n = 3$. (C) The TEM image showing the morphology of OMVs (scale bar: 100 nm). (D) SDS-PAGE of *Salmonella* and *Salmonella* derived OMVs. (E) Drug loading efficiency and encapsulation efficiency of OMVs/DOX at different drug feeding ratios. (F) The fluorescence intensity of DOX, OMVs and OMVs/DOX. (G) The drug release profile of OMVs/DOX under different pH conditions. (H) CLSM images of neutrophils and HUVEC cells incubated with PBS, DOX, or OMVs/DOX for 1 h (Scale bar = 20 μm). (I) The cell viability of DOX and OMVs/DOX against C6 cells evaluated by MTT assay. $n = 6$. (J) Antibacterial activity of DOX and OMVs/DOX. $n = 3$. (K) IC$_{50}$ of DOX and OMVs/DOX towards tumor cells and bacteria. Data are presented as mean ± SD.

(Fig. 2G and H). Next, we tested whether such high level of neutrophil infiltration could promote tumor-targeted delivery of OMVs/DOX. The OMVs/DOX was intravenously injected at 48 h post-administration of bacteria, and the mice were sacrificed to collected main organs. Benefited from the intrinsic fluorescence of DOX, the biodistribution of OMVs/DOX was conveniently visualized by *ex vivo* IVIS image (Fig. 2I). As the major drug metabolism/elimination organs, both liver and kidneys emitted bright fluorescence. Specifically, we focused our attention on brain tissue, and no fluorescence was found after single injection of free

DOX or OMVs/DOX, ascribed to the BBB that prevents drug penetration into the brain. Such biological barrier is the critical limitation to most anti-glioma drugs. Notably, the combination of *S.t*-ΔpG^{FlaB} and OMVs/DOX showed a remarkable fluorescence at brain tumor site, suggesting the successful BBB penetration and tumor-targeted delivery. In contrast, the fluorescence in the brain was still rather weak when combining *S.t*-ΔpG^{FlaB} and free DOX. Therefore, the OMV carrier was important for DOX delivery, which can be loaded into neutrophils *via* TLR4-mediated recognition and then transported into bacteria-colonized tumor *via*
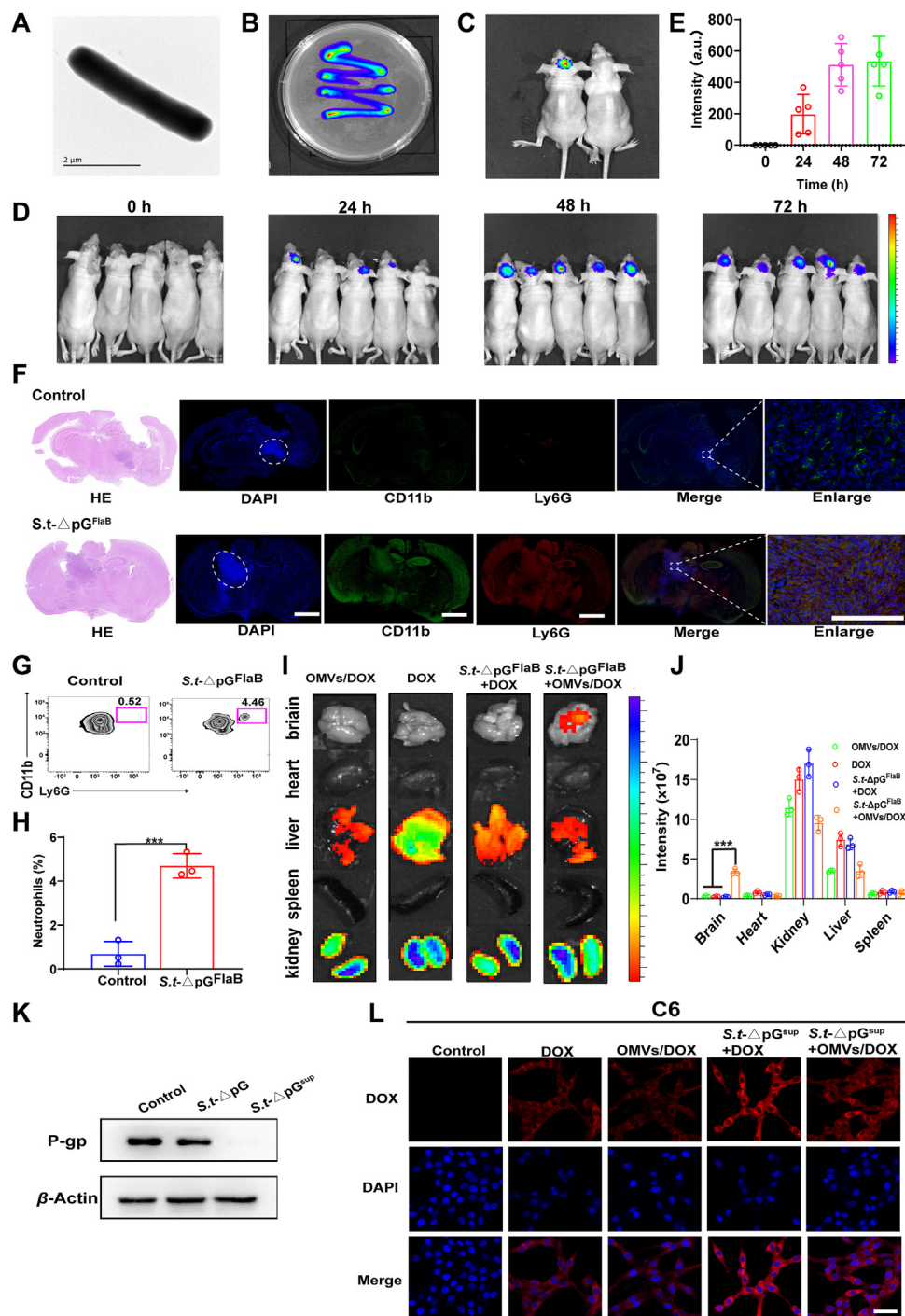
Figure 2 "Trojan horse" bacteria to facilitate the tumor targeting delivery of OMVs/DOX and reverse drug resistance. (A) TEM image of *S.t*-ΔpG. (B) Bacterial bioluminescence in agar plate. (C) Biodistribution of *S.t*-ΔpG in normal and C6 tumor-bearing nude mice at 48 h post injection. (D) Dynamic monitoring bioluminescence of *S.t*-ΔpG *in vivo*, and (E) quantified fluorescence intensity at tumor tissue. $n = 5$. (F) H&E and immunofluorescence co-staining of neutrophil infiltration into tumor tissue at 48 h after *S.t*-ΔpG^{FlaB} treatment. The white circle indicates the tumor tissue. The scale bar was 500 μm, and the enlarged scale bar was 50 μm. (G) Flow cytometry and (H) intensity quantification of the CD11b/Ly6G fluorescence to analyze the neutrophil infiltration. $n = 3$. ***$P < 0.001$. (I) *Ex vivo* IVIS images of DOX accumulation in major organs at 8 h after various treatments. (J) Quantitative analysis of the fluorescent in different organs. Data are represented as mean ± standard deviation. $n = 3$. ***$P < 0.001$. (K) *S.t*-ΔpG^{sup} induced P-gp down-regulation. C6 cells were treated with PBS, *S.t*-ΔpG^{FlaB} or *S.t*-ΔpG^{FlaB} supernatant (*S.t*-ΔpG^{sup}). (L) Fluorescence images showing the intracellular accumulation of DOX in C6 cells after various treatments. C6 cells were treated with culture medium, DOX, OMVs/DOX, S.t-ΔpG^{sup} + DOX, or S.t-ΔpG^{sup} + OMVs/DOX, respectively (scale bar = 20 μm). Data are presented as mean ± SD.

neutrophil infiltration. We further quantified the intensity, and *S.t*-ΔpG^{FlaB} + OMVs/DOX could achieve about 18-fold enhancement of drug accumulation into brain as compared to the other groups (Fig. 2J).

After tumor-targeted delivery, the next critical step for chemotherapy is effective accumulation into tumor cells. While various nanomedicines have been equipped with specific ligands to achieve effective internalization into tumor cells, the cunning tumor cells could still resist drugs treatment by up-regulation of the multidrug resistance transporter P-glycoprotein (P-gp). P-gp pumps out drugs from cells and thus compromises the therapeutic outcome. Fortunately, previous work has indicated *Salmonella* can downregulate P-gp through the *Salmonella* type III secretion effector[63], and we therefore expected the tumor colonized *S.t*-ΔpG^{FlaB} could reverse DOX resistance. To test this, the culturing media of *S.t*-ΔpG^{FlaB} were collected *via* centrifugation, and then incubated with C6 tumor cells for 24 h. Based on the WB analysis, the cells showed a high level of P-gp, while the protein was almost completely suppressed upon treatment with the *S.t*-ΔpG^{FlaB} supernatant (termed *S.t*-ΔpG^{sup}) (Fig. 2K). The *S.t*-ΔpG precipitant, however, did not show much influence on P-gp expression, confirming the mechanism of P-gp down-regulation *via* secretion effector. The secretion protein of SipA is the key factor responsible for P-gp regulation, which interacts with a transmembrane receptor to induce a CASP3 dependent cleavage of P-gp[63]. We next explored the benefits of P-gp inhibition on DOX delivery and anti-tumor efficacy. After incubation with free DOX and OMVs/DOX, red fluorescence was clearly seen inside cells owing to drug internalization (Fig. 2L, Supporting Information Fig. S3). However, such fluorescence was strongly intensified when the cells were pre-treated with the supernatant of *S.t*-ΔpG^{FlaB}, attributable to P-gp downregulation through bacteria secretion effector to block drug efflux. As a result, an enhanced anti-tumor effect was observed for DOX upon combination with *S.t*-ΔpG^{FlaB} supernatant (Supporting Information Fig. S4).

3.3. Tumor microenvironment regulation effect of the bacteria

In addition to promoting drug delivery, another function of bacteria is to modulate tumor immune microenvironment (TIE). It is known that TIE has a strong influence on tumor progression, growth, metastasis, as well as the anti-tumor efficacy of various treatment modalities[64,65]. In established glioma tissue, macrophages are the most abundant immune cells, which are mainly polarized into M2 phenotype to promote tumor growth[66,67]. Therefore, repolarization of M2 macrophage into M1 phenotype is a highly promising strategy to remodel TIE for enhanced anti-tumor effect. To achieve such goal, we tagged the *FlaB* gene into bacteria, which is an excellent adjuvant for immunoregulation to activate innate immune responses *via* Toll-like receptor 5 (TLR5) signaling pathway[49]. The *FlaB* gene was cloned into pBAD plasmid vector by fusing pelB leader sequence to the upstream of flaB to guide extracellular secretion, in which the gene expression from plasmid [pBAD-pelB-FlaB (pFlaB)] was induced in the presence of ʟ-arabinose (Fig. 3A). After system construction, the potential of bacteria to educate macrophage was evaluated by measuring the typical phenotype biomarkers, including CD80 (M1 marker) and CD206 (M2 marker). At cellular level, the RAW264.7 cells were employed as a macrophage model, which were initially polarized into M2 phenotype with IL-4 pre-incubation. After *S.t*-ΔpG treatment, an obvious upregulation of CD80 and decrease of CD206 was observed (Fig. 3B), demonstrating the M2-to-M1 phenotype

switch. Such effect was further strengthened upon treatment with *S.t*-ΔpG^{FlaB}, consistent with previous report that the excretion of FlaB promotes M1 macrophage polarization[48]. To further validate this result, the surface CD80/CD206 expression was measured by flow cytometry, and the intensity was quantified (Fig. 3C−F). After bacteria treatment, the fluorescence of CD80 became stronger accompanied by reduce level of CD206, in which the general trend was in agreement with the above protein expression results.

Motivated by the above result, we then studied the TIE modulation activity of the bacteria *in vivo* by using orthotopic glioma model. To visualize the macrophage polarization, CD86 and CD206 were stained by green and red fluorescence, respectively. A notable red fluorescence of CD206 was observed at the tumor while the green fluorescence of CD86 was rather weak (Fig. 3G). This can be explained by the immune suppressive microenvironment of tumor where the tumor associated macrophages are mainly polarized into pro-inflammatory M2 phenotype. Interestingly, the bacteria treatment could effectively promote the macrophage polarization into M1 phenotype, as evidenced by the increase of CD86 fluorescence and reduction of CD206 signal. For quantitative analysis, the fluorescence-activated cell sorting (FACS) was performed to count each phenotype of macrophage (Fig. 3H−J). After *S.t*-ΔpG^{FlaB} therapy, the M1/M2 amount ratio improved by about 20-fold, and the amount of M1 macrophages markedly increased from 16.07% to 47.27%. Notably, the M1 polarized macrophages could restore their anti-tumor activity by both innate (*e.g.*, engulfing tumor cells, excreting anti-tumor cytokines) and adaptive (*e.g.*, antigen presentation) immunity, thus promoting the final therapeutic efficacy[68,69].

3.4. The combination of Salmonella and OMVs/DOX inhibits the growth of glioma in vivo

Having demonstrated the tumor-targeted delivery of OMVs/DOX and tumor microenvironment regulation effect of *S.t*-ΔpG^{FlaB}, we then investigated the anti-tumor activity of their combination. After intracranial injection of tumor cells to develop orthotopic glioma model, the mice were randomly divided into 6 groups, each receiving one of the following treatments (Fig. 4A): (1) PBS; (2) OMVs/DOX, (3) *S.t*-ΔpG^{FlaB}, (4) free DOX, (5) *S.t*-ΔpG^{FlaB} + free DOX, and (6) *S.t*-ΔpG^{FlaB} + OMVs/DOX. To monitor the tumor process, a luciferase-expressing isogenic C6 cell line was employed, and the dynamic tumor growth was visualized *via* an IVIS imaging system (Fig. 4B and C). For the PBS control, the bioluminescence in brain gradually intensified, indicating a rapid growth of tumor. Three mice died on Day 20 and all of the mice died on Day 25 due to the high mortality of glioma. Interestingly, free DOX achieved considerably higher tumor inhibition effect than that of OMVs/DOX. The single injection of *S.t*-ΔpG^{FlaB} also suppressed tumor to some extent, owing to the intrinsic anti-tumor effect *via* different mechanisms, such as systematically modulating the TIM and nutrition competition with tumor tissue[42,70]. For example, we have demonstrated the macrophages repolarization activity of *S.t*-ΔpG^{FlaB}. To confirm the bacteria-mediated immunotherapy, several representative anti-tumor cytokines (IL-6, TNF-α, and IL-12) and chemotactic factor (CXCL10) in serum were measured, all of which were elevated after treatment with *S.t*-ΔpG^{FlaB}-containing groups (Fig. 4D). Note that the efficacy was further enhanced by combining *S.t*-ΔpG^{FlaB} and free DOX, suggesting a synergistic effect. This can be ascribed to the P-gp down-regulation activity of *S.t*-ΔpG^{FlaB} to sensitize the DOX efficacy. Among them, *S.t*-
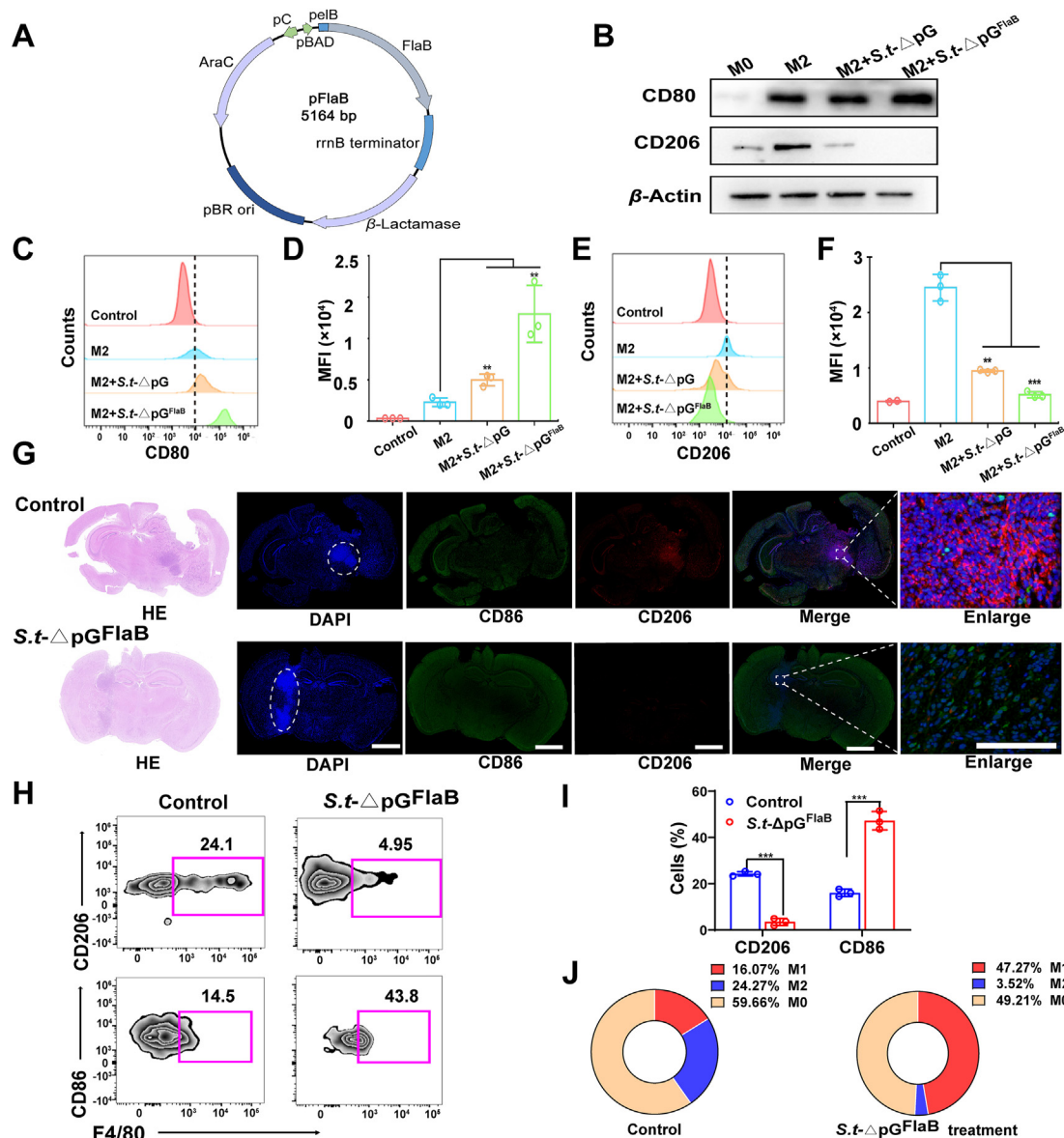
Figure 3 Functions of *S.t*-ΔpG^{FlaB} to modulate tumor immune microenvironment. (A) Schematic illustration of the engineered plasmid pFlaB. bp, base pair. (B) Protein expression of M1 macrophage marker CD80 and M2 macrophage marker CD206 after various treatments. Flow cytometry (C, E) and the quantified intensity (D, F) of CD80 and CD206 after various treatments. $n = 3$. $**P < 0.01$, $***P < 0.001$. G) H&E staining and CD86/CD206 fluorescence co-staining to assess the macrophage polarization in tumor tissue at 48 h after *S.t*-ΔpG^{FlaB} treatment. The white circle indicates the tumor tissue. The scale bar is 500 μm, and the enlarged scale bar is 50 μm. The sample was from the same mouse as that in Fig. 2f but different sections. (H−J) Flow cytometry and intensity quantification to analyze the polarization of macrophages. $n = 3$. Data are presented as mean ± SD. $**P < 0.01$; $***P < 0.001$.

ΔpG^{FlaB} plus OMVs/DOX achieved the best tumor suppression effect. On Day 25 post-treatment, the tumor was completely eradicated in four mice, and one remaining mouse only emitted marginal signal.

To accurately monitor the tumor growth *in vivo*, T$_1$-weighted magnetic resonance imaging (T1W-MRI) of mouse brains was scanned on Day 15 (Fig. 5E), through which the tumor tissue can be clearly seen in the brain. Compared to the PBS control, all DOX and bacteria groups could inhibit tumor growth to certain extent, and obviously, the best efficacy was seen for *S.t*-ΔpG^{FlaB} plus OMVs/DOX group, with obvious inhibition of tumor in

samples. We then calculated the survival rate, the most important parameter to evaluate the treatment outcome (Fig. 5F). Notably, all mice were still alive on Day 25 after *S.t*-ΔpG^{FlaB} plus OMVs/DOX therapy, while none of the other treatments could have all mice survived, giving the relative efficacy of *S.t*-ΔpG^{FlaB} + OMVs/DOX > *S.t*-ΔpG^{FlaB} + DOX > *S.t*-ΔpG^{FlaB} > DOX > OMVs/DOX > Control. After treatment, the mice were sacrificed and the tumor tissue was extracted to directly evaluate the tumor suppression effect, and again, *S.t*-ΔpG^{FlaB} plus OMVs/DOX group displayed the best efficacy, achieving complete tumor ablation.
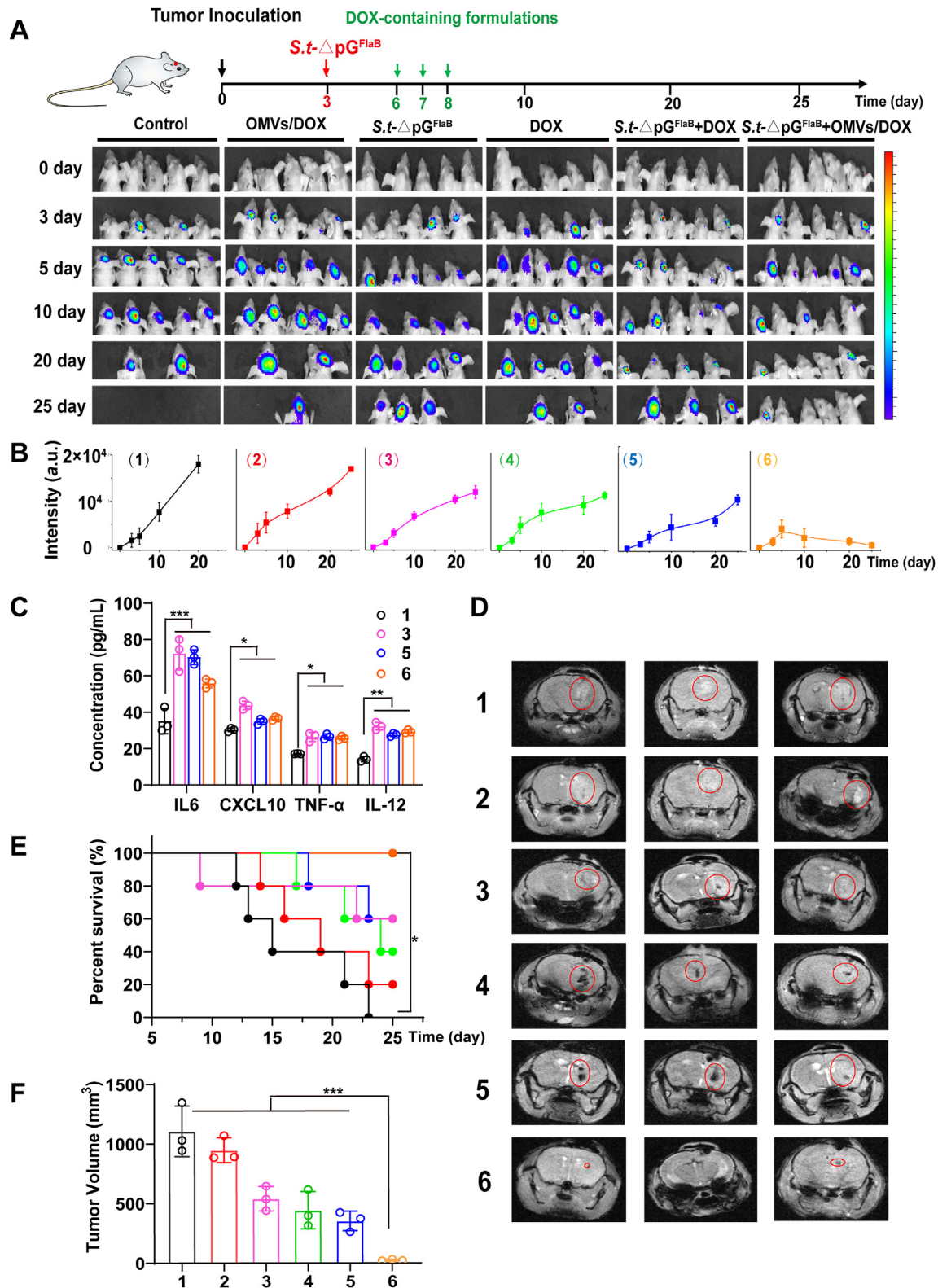
Figure 4 Antitumor efficacy on nude mice bearing C6 glioma. (A) Schematic describing the time course of establishment of an orthotopic brain tumor model in mice and treatment regimen. (B) IVIS images and fluorescence quantification indicating the dynamic tumor growth after various treatments. $n = 5$. (C) ELISA analysis the level of IL-6, CXCL10, TNF-α, IL-12 in serum after various treatments. $n = 3$. (D) T1W-MRI imaging of glioma in mice on Day 15 after various treatments. The red circle indicates the tumor tissue. (E) Survival rate of mice and (F) tumor volume after various treatments. 1 (black): the control; 2 (red): OMVs/DOX; 3 (pink): *S.t*-ΔpG^{FlaB}; 4 (green): free DOX; 5 (blue): *S.t*-ΔpG^{FlaB} + DOX; 6 (orange): *S.t*-ΔpG^{FlaB} + OMVs/DOX. Data are presented as mean ± SD. *$P < 0.05$, **$P < 0.01$, ***$P < 0.001$.
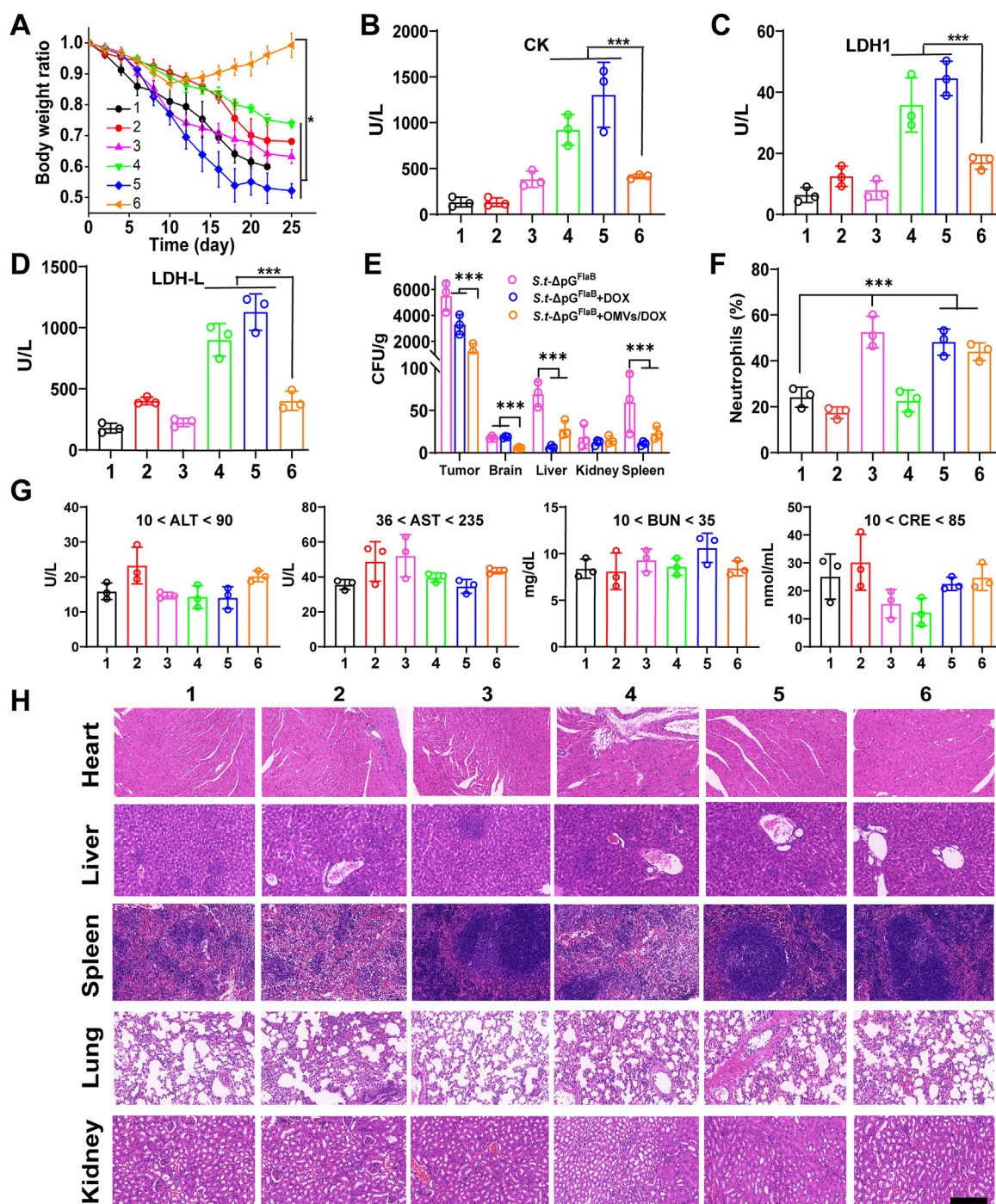
Figure 5 Biosafety evaluation of various treatments. (A) Dynamic monitoring of the body weight of the mice during various treatments. $n = 5$. (B−D) Myocardial enzyme spectrum data of mice after various treatments. $n = 3$. (E) The bacteria colonization in tumor, brain, spleen, liver, and kidneys after different treatments. $n = 3$. (F) Ratio of neutrophils/leukocytes in blood after various treatments. $n = 3$. (G) The hepatotoxicity and nephrotoxicity of each treatment by measuring the levels of ALT, AST, BUN, and CRE. $n = 3$. (H) Histological analysis of the major organs slices after various treatments (scale bar: 30 μm). 1 (black): the control; 2 (red): OMVs/DOX; 3 (pink): $S.t$-ΔpG^{FlaB}; 4 (green): free DOX; 5 (blue): $S.t$-ΔpG^{FlaB} + DOX; 6 (orange): $S.t$-ΔpG^{FlaB} + OMVs/DOX. Data are presented as mean ± SD. *$P < 0.05$, **$P < 0.01$, ***$P < 0.001$.

3.5. In vivo biocompatibility and biosafety evaluation

Finally, the biosafety of various treatments was investigated. All formulations showed less than 5% hemolysis (Supporting Information Fig. S5), confirming their comparability for intravenous injection. The body weight was the most direct index to reflect the health condition of mice (Fig. 5A). Along with tumor growth, the mice with PBS control showed a progressive decrease of body weight, indicating the exacerbation of health condition. Among various treatments, only $S.t$-ΔpG^{FlaB} plus OMVs/DOX could

rescue the body weight loss, and even an increase in body weight was observed after 10 days. Specifically, DOX-based chemotherapy may cause cardiotoxicity[71], while bacterial therapy has an infection risk[72]. We then tested these two factors side-by-side. For free DOX treatment group, a significant increase of creatine kinase (CK) (Fig. 5B) and lactate dehydrogenase (LDH1, LDH-L) (Fig. 5C and D) were observed, indicating a strong cardiotoxicity. After encapsulation into OMVs, such indexes were within normal level after treatment, confirming the advantage of OMVs vehicles to decrease the potential side effects of DOX. Therefore, the nanosystem may not improve the therapeutic efficacy, but can minimize the potential side effects. The $S.t$-ΔpG$^{\text{FlaB}}$ injection groups, on the other hand, showed a large amount of bacteria colonization in tumor tissue (Fig. 5E), and the blood neutrophils also increased significantly (Fig. 5F), which laid the basis for neutrophils mediated tumor homing of OMVs/DOX. However, non-specific distribution and colonization of bacteria was also noticed in brain, spleen and liver upon single administration of $S.t$-ΔpG$^{\text{FlaB}}$, which may cause the risk of infection-related side effects. The combination of $S.t$-ΔpG$^{\text{FlaB}}$ and OMVs/DOX, by contrast, could minimize such potential with markedly reduced bacteria levels in different normal organs. In addition, the LPS content in serum (Supporting Information Fig. S6) and infection-related cytokines (TNF-α and IL-6) in major organs (Supporting Information Fig. S7) were measured, in which the combination of DOX or OMVs/DOX could significantly decrease the endotoxin activity of $S.t$-ΔpG$^{\text{FlaB}}$ treatment, indicating the detoxification effect on DOX on bacteria. Collectively, the combination of $S.t$-ΔpG$^{\text{FlaB}}$ and OMVs/DOX not only decreased side effects of DOX *via* targeted drug delivery, but also cleared the bacteria by DOX-induced disinfection, demonstrating the superiority of such combination in terms of biocompatibility. Moreover, we also measured several other routine biochemical parameters, including serum alanine transaminase (ALT), aspartate transaminase (AST), blood urea nitrogen (BUN), serum creatinine (CRE) (Fig. 5G), while none of these indexes showed any significant change after different therapies, suggesting the lack of hepatotoxicity and nephrotoxicity. Finally, major organs of the mice were collected for H&E staining, while no pathological change was observed after various treatments (Fig. 5H), indicating the lack of acute organ damage of various treatments.

4. Conclusions

In summary, we have developed a bacteria-based drug delivery system to address the key limitations of glioma chemotherapy. On the one hand, the bioengineered $S.t$-ΔpG$^{\text{FlaB}}$ was fabricated to effectively colonize into glioma tissue, which acted as Trojan horse to regulate tumor microenvironment, including macrophage repolarization, neutrophil recruitment, as well as P-gp down-regulation on glioma cell surface. On the other hand, the $S.t$-ΔpG$^{\text{FlaB}}$ derived OMVs were employed as loading cargo of DOX. OMVs could encapsulate DOX with high efficiency, and more importantly, hitchhike circulating neutrophils to enable BBB/BTB bypassing and tumor-targeted accumulation. Compared to traditional nanoparticles that rely on EPR effect or surface modifications for tumor-targeted delivery, such chemotaxis mimic strategy is much more efficient in a spontaneous manner. During this process, bacteria-induced inflammation was critically important, as evidenced by the significantly enhanced drug accumulation of $S.t$-ΔpG$^{\text{FlaB}}$ + OMVs/DOX in tumor than both $S.t$-

ΔpG$^{\text{FlaB}}$ + DOX and OMVs/DOX groups, confirming the contribution of neutrophil mediated hitchhiking delivery. The OMVs/DOX delivery of DOX showed robust anti-tumor effect with almost complete tumor eradication. This efficacy was superior to the previously reported neutrophil-mediated drug delivery system owing to the P-gp suppression effect of bacteria to reverse drug resistance[40]. Moreover, such targeted drug delivery system not only minimized potential side-effects of DOX, but also decreased the key safety risk of bacteria-mediated tumor therapy, *i.e.*, bacterial infection. Overall, this work provides an effective tumor microenvironment regulation method to enable brain tumor-targeted delivery of drug *via* neutrophil hitchhiking for enhanced glioma therapy with excellent biocompatibility.

Author contributions

Pengfei Rong, Wenhu Zhou designed the research. Ze Mi and Qing Yao carried out the experiments and performed data analysis. Jiahao Liu and Hongpei Tan participated part of the experiments. Xiaoqian Ma and Yan Qi provided experimental drugs and quality control. Ze Mi and Qingyao wrote the manuscript. Xiaoyuan Chen, Wenhu Zhou, Pengfei Rong, Jinghai Zheng, Zhengguo Liu revised the manuscript. All of the authors have read and approved the final manuscript.

Conflicts of interest

The authors confirm that this article content has no conflict of interest.

Appendix A. Supporting information

Supporting data to this article can be found online at https://doi.org/10.1016/j.apsb.2022.09.016.

References

1. Bi J, Chowdhry S, Wu S, Zhang W, Masui K, Mischel PS. Altered cellular metabolism in gliomas—an emerging landscape of actionable co-dependency targets. *Nat Rev Cancer* 2020;**20**:57−70.
2. Venkataramani V, Tanev DI, Strahle C, Studier-Fischer A, Fankhauser L, Kessler T, et al. Glutamatergic synaptic input to glioma cells drives brain tumour progression. *Nature* 2019;**573**:532−8.
3. Qiao C, Yang J, Shen Q, Liu R, Li Y, Shi Y, et al. Traceable nanoparticles with dual targeting and ROS Response for RNAi-based immunochemotherapy of intracranial glioblastoma treatment. *Adv Mater* 2018;**30**:e1705054.
4. Zhang J, Chen C, Li A, Jing W, Sun P, Huang X, et al. Immunostimulant hydrogel for the inhibition of malignant glioma relapse post-resection. *Nat Nanotechnol* 2021;**16**:538−48.

5. Touat M, Li YY, Boynton AN, Spurr LF, Iorgulescu JB, Bohrson CL, et al. Mechanisms and therapeutic implications of hypermutation in gliomas. *Nature* 2020;**580**:517−23.

6. Jin MS, Oldham ML, Zhang Q, Chen J. Crystal structure of the multidrug transporter P-glycoprotein from Caenorhabditis elegans. *Nature* 2012;**490**:566−9.

7. Chen H, Zhou M, Zeng Y, Miao T, Luo H, Tong Y, et al. Biomimetic lipopolysaccharide-free bacterial outer membrane-functionalized nanoparticles for brain-targeted drug delivery. *Adv Sci* 2022:2105854.

8. Wei Y, Sun Y, Wei J, Qiu X, Meng F, Storm G, et al. Selective transferrin coating as a facile strategy to fabricate BBB-permeable and targeted vesicles for potent RNAi therapy of brain metastatic breast cancer in vivo. *J Control Release* 2021;**337**:521−9.

9. Ni J, Miao T, Su M, Khan NU, Ju X, Chen H, et al. PSMA-targeted nanoparticles for specific penetration of blood−brain tumor barrier and combined therapy of brain metastases. *J Control Release* 2021;**329**:934−47.

10. Guo Q, Zhu Q, Miao T, Tao J, Ju X, Sun Z, et al. LRP1-upregulated nanoparticles for efficiently conquering the blood−brain barrier and targetedly suppressing multifocal and infiltrative brain metastases. *J Control Release* 2019;**303**:117−29.

11. Khan NU, Ni J, Ju X, Miao T, Chen H, Han L. Escape from abluminal LRP1-mediated clearance for boosted nanoparticle brain delivery and brain metastasis treatment. *Acta Pharm Sin B* 2021;**11**:1341−54.

12. Wang H, Chao Y, Zhao H, Zhou X, Zhang F, Zhang Z, et al. Smart nanomedicine to enable crossing blood−brain barrier delivery of checkpoint blockade antibody for immunotherapy of glioma. *ACS Nano* 2022;**16**:664−74.

13. Yu M, Su D, Yang Y, Qin L, Hu C, Liu R, et al. D-T7 peptide-modified PEGylated bilirubin nanoparticles loaded with cediranib and paclitaxel for antiangiogenesis and chemotherapy of glioma. *ACS Appl Mater Interfaces* 2019;**11**:176−86.

14. Ruan S, Qin L, Xiao W, Hu C, Zhou Y, Wang R, et al. Acid-responsive transferrin dissociation and GLUT mediated exocytosis for increased blood−brain barrier transcytosis and programmed glioma targeting delivery. *Adv Funct Mater* 2018;**28**:1802227.

15. Ruan S, Xie R, Qin L, Yu M, Xiao W, Hu C, et al. Aggregable nanoparticles-enabled chemotherapy and autophagy inhibition combined with anti-PD-L1 antibody for improved glioma treatment. *Nano Lett* 2019;**19**:8318−32.

16. Ruan S, Zhou Y, Jiang X, Gao H. Rethinking CRITID procedure of brain targeting drug delivery: circulation, blood brain barrier recognition, intracellular transport, diseased cell targeting, internalization, and drug release. *Adv Sci* 2021;**8**:2004025.

17. Gao H. Progress and perspectives on targeting nanoparticles for brain drug delivery. *Acta Pharm Sin B* 2016;**6**:268−86.

18. Feng J, Lepetre-Mouelhi S, Gautier A, Mura S, Cailleau C, Coudore F, et al. A new painkiller nanomedicine to bypass the blood−brain barrier and the use of morphine. *Sci Adv* 2019;**5**:eaau5148.

19. Lin T, Zhao P, Jiang Y, Tang Y, Jin H, Pan Z, et al. Blood−brain-barrier-penetrating albumin nanoparticles for biomimetic drug delivery *via* albumin-binding protein pathways for antiglioma therapy. *ACS Nano* 2016;**10**:9999−10012.

20. Wu H, Lu H, Xiao W, Yang J, Du H, Shen Y, et al. Sequential targeting in crosslinking nanotheranostics for tackling the multibarriers of brain tumors. *Adv Mater* 2020;**32**:e1903759.

21. Matsumura Y. Preclinical and clinical studies of NK012, an SN-38-incorporating polymeric micelles, which is designed based on EPR effect. *Adv Drug Deliv Rev* 2011;**63**:184−92.

22. Farshbaf M, Valizadeh H, Panahi Y, Fatahi Y, Chen M, Zarebkohan A, et al. The impact of protein corona on the biological behavior of targeting nanomedicines. *Int J Pharm* 2022:121458.

23. Xiao W, Wang Y, Zhang H, Liu Y, Xie R, He X, et al. The protein corona hampers the transcytosis of transferrin-modified nanoparticles through blood−brain barrier and attenuates their targeting ability to brain tumor. *Biomaterials* 2021;**274**:120888.

24. Wang Y, Zhang H, Xiao W, Liu Y, Zhou Y, He X, et al. Unmasking CSF protein corona: effect on targeting capacity of nanoparticles. *J Control Release* 2021;**333**:352−61.

25. Im S, Jang D, Saravanakumar G, Lee J, Kang Y, Lee YM, et al. Harnessing the formation of natural killer-tumor cell immunological synapses for enhanced therapeutic effect in solid tumors. *Adv Mater* 2020;**32**. e2000020.

26. Qi J, Jin F, You Y, Du Y, Liu D, Xu X, et al. Synergistic effect of tumor chemo-immunotherapy induced by leukocyte-hitchhiking thermal-sensitive micelles. *Nat Commun* 2021;**12**:4755.

27. Mantovani A, Allavena P, Sica A, Balkwill F. Cancer-related inflammation. *Nature* 2008;**454**:436−44.

28. Hegde S, Krisnawan VE, Herzog BH, Zuo C, Breden MA, Knolhoff BL, et al. Dendritic cell paucity leads to dysfunctional immune surveillance in pancreatic cancer. *Cancer Cell* 2020;**37**:289−307.e9.

29. Ding J, Sui D, Liu M, Su Y, Wang Y, Liu M, et al. Sialic acid conjugate-modified liposomes enable tumor homing of epirubicin *via* neutrophil/monocyte infiltration for tumor therapy. *Acta Biomater* 2021;**134**:702−15.

30. Vishnevskiy DA, Garanina AS, Chernysheva AA, Chekhonin VP, Naumenko VA. Neutrophil and nanoparticles delivery to tumor: is it going to carry that weight?. *Adv Healthcare Mater* 2021;**10**:2002071.

31. Wang J, Tang W, Yang M, Yin Y, Li H, Hu F, et al. Inflammatory tumor microenvironment responsive neutrophil exosomes-based drug delivery system for targeted glioma therapy. *Biomaterials* 2021;**273**:120784.

32. Subhan MA, Torchilin VP. Neutrophils as an emerging therapeutic target and tool for cancer therapy. *Life Sci* 2021;**285**:119952.

33. Kang T, Zhu Q, Wei D, Feng J, Yao J, Jiang T, et al. Nanoparticles coated with neutrophil membranes can effectively treat cancer metastasis. *ACS Nano* 2017;**11**:1397−411.

34. Binnewies M, Roberts EW, Kersten K, Chan V, Fearon DF, Merad M, et al. Understanding the tumor immune microenvironment (TIME) for effective therapy. *Nat Med* 2018;**24**:541−50.

35. Keren L, Bosse M, Marquez D, Angoshtari R, Jain S, Varma S, et al. A structured tumor-immune microenvironment in triple negative breast cancer revealed by multiplexed ion beam imaging. *Cell* 2018;**174**:1373−1387.e19.

36. Li M, Li S, Zhou H, Tang X, Wu Y, Jiang W, et al. Chemotaxis-driven delivery of nano-pathogenoids for complete eradication of tumors post-phototherapy. *Nat Commun* 2020;**11**:1126.

37. Li Y, Han Y, Su R, Liu Y, Chong G, Xu D, et al. Photosensitizer-laden neutrophils are controlled remotely for cancer immunotherapy. *Cell Rep* 2020;**33**:108499.

38. Li M, Xie D, Tang X, Yang C, Shen Y, Zhou H, et al. Phototherapy facilitates tumor recruitment and activation of natural killer T cells for potent cancer immunotherapy. *Nano Lett* 2021;**21**:6304−13.

39. Chu D, Dong X, Shi X, Zhang C, Wang Z. Neutrophil-based drug delivery systems. *Adv Mater* 2018;**30**:1706245.

40. Xue J, Zhao Z, Zhang L, Xue L, Shen S, Wen Y, et al. Neutrophil-mediated anticancer drug delivery for suppression of postoperative malignant glioma recurrence. *Nat Nanotechnol* 2017;**12**:692−700.

41. Mi Z, Guo L, Liu P, Qi Y, Feng Z, Liu J, et al. "Trojan horse" *Salmonella* enabling tumor homing of silver nanoparticles *via* neutrophil infiltration for synergistic tumor therapy and enhanced biosafety. *Nano Lett* 2021;**21**:414−23.

42. Mi Z, Feng ZC, Li C, Yang X, Ma MT, Rong PF. *Salmonella*-mediated cancer therapy: an innovative therapeutic strategy. *J Cancer* 2019;**10**:4765.

43. Huang X, Pan J, Xu F, Shao B, Wang Y, Guo X, et al. Bacteria-based cancer immunotherapy. *Adv Sci* 2021;**8**:2003572.

44. Felgner S, Kocijancic D, Frahm M, Curtiss III R, Erhardt M, Weiss S. Optimizing *Salmonella* enterica serovar *Typhimurium* for bacteria-mediated tumor therapy. *Gut Microb* 2016;**7**:171−7.

45. Pang B, Neefjes J. Coupled for cross-presentation in tumor immuno-therapy. *Sci Transl Med* 2010;**2**. 44ps0-ps0.

46. Kurtz JR, Goggins JA, McLachlan JB. *Salmonella* infection: interplay between the bacteria and host immune system. *Immunol Lett* 2017;**190**:42−50.

47. Westphal K, Leschner S, Jablonska J, Loessner H, Weiss S. Containment of tumor-colonizing bacteria by host neutrophils. *Cancer Res* 2008;**68**:2952−60.

48. Zheng JH, Nguyen VH, Jiang SN, Park SH, Tan W, Hong SH, et al. Two-step enhanced cancer immunotherapy with engineered *Salmonella typhimurium* secreting heterologous flagellin. *Sci Transl Med* 2017;**9**.

49. Nguyen CT, Hong SH, Sin JI, Vu HVD, Jeong K, Cho KO, et al. Flagellin enhances tumor-specific CD8$^+$ T cell immune responses through TLR5 stimulation in a therapeutic cancer vaccine model. *Vaccine* 2013;**31**:3879−87.

50. Lee SE, Kim SY, Jeong BC, Kim YR, Bae SJ, Ahn OS, et al. A bacterial flagellin, *Vibrio vulnificus* FlaB, has a strong mucosal adjuvant activity to induce protective immunity. *Infect Immun* 2006;**74**: 694−702.

51. Li M, Zhou H, Yang C, Wu Y, Zhou X, Liu H, et al. Bacterial outer membrane vesicles as a platform for biomedical applications: an update. *J Control Release* 2020;**323**:253−68.

52. Peng LH, Wang MZ, Chu Y, Zhang L, Niu J, Shao H-T, et al. Engineering bacterial outer membrane vesicles as transdermal nanoplatforms for photo-TRAIL-programmed therapy against melanoma. *Sci Adv* 2020;**6**:eaba2735.

53. Liu L, Wu J, Gao J, Lu X. Bacteria-derived nanoparticles: multifunctional containers for diagnostic and therapeutic applications. *Adv Healthcare Mater* 2020;**9**:2000893.

54. Nicolás-Ávila JÁ, Adrover JM, Hidalgo A. Neutrophils in homeostasis, immunity, and cancer. *Immunity* 2017;**46**:15−28.

55. Kolaczkowska E, Kubes P. Neutrophil recruitment and function in health and inflammation. *Nat Rev Immunol* 2013;**13**:159−75.

56. Toyofuku M, Nomura N, Eberl L. Types and origins of bacterial membrane vesicles. *Nat Rev Microbiol* 2019;**17**:13−24.

57. Kuang H, Ku SH, Kokkoli E. The design of peptide-amphiphiles as functional ligands for liposomal anticancer drug and gene delivery. *Adv Drug Delivery Rev* 2017;**110**:80−101.

58. Jiang SN, Park SH, Lee HJ, Zheng JH, Kim HS, Bom HS, et al. Engineering of bacteria for the visualization of targeted delivery of a cytolytic anticancer agent. *Mol Ther* 2013;**21**:1985−95.

59. Nemunaitis J, Cunningham C, Senzer N, Kuhn J, Cramm J, Litz C, et al. Pilot trial of genetically modified, attenuated *Salmonella* expressing the *E. coli* cytosine deaminase gene in refractory cancer patients. *Cancer Gene Ther* 2003;**10**:737−44.

60. Thamm DH, Kurzman ID, King I, Li Z, Sznol M, Dubielzig RR, et al. Systemic administration of an attenuated, tumor-targeting *Salmonella typhimurium* to dogs with spontaneous neoplasia: phase I evaluation. *Clin Cancer Res* 2005;**11**:4827−34.

61. Wen M, Zheng JH, Choi JM, Pei J, Li CH, Li SY, et al. Genetically-engineered *Salmonella typhimurium* expressing TIMP-2 as a therapeutic intervention in an orthotopic glioma mouse model. *Cancer Lett* 2018;**433**:140−6.

62. Momiyama M, Zhao M, Kimura H, Tran B, Chishima T, Bouvet M, et al. Inhibition and eradication of human glioma with tumor-targeting *Salmonella typhimurium* in an orthotopic nude-mouse model. *Cell Cycle* 2012;**11**:628−32.

63. Mercado-Lubo R, Zhang Y, Zhao L, Rossi K, Wu X, Zou Y, et al. A *Salmonella* nanoparticle mimic overcomes multidrug resistance in tumours. *Nat Commun* 2016;**7**:12225.

64. Saeed M, Chen F, Ye J, Shi Y, Lammers T, De Geest BG, et al. From design to clinic: engineered nanobiomaterials for immune normalization therapy of cancer. *Adv Mater* 2021:2008094.

65. Song Y, Huang Y, Zhou F, Ding J, Zhou W. Macrophage-targeted nanomedicine for chronic diseases immunotherapy. *Chin Chem Lett* 2021;**33**:597−612.

66. Chen Z, Hambardzumyan D. Macrophage-tumor cell intertwine drives the transition into a mesenchymal-like cellular state of glioblastoma. *Cancer Cell* 2021;**39**:743−5.

67. Gao X, Li S, Ding F, Liu X, Wu Y, Li J, et al. A virus-mimicking nucleic acid nanogel reprograms microglia and macrophages for glioblastoma therapy. *Adv Mater* 2021;**33**:e2006116.

68. Elmore MR, Najafi AR, Koike MA, Dagher NN, Spangenberg EE, Rice RA, et al. Colony-stimulating factor 1 receptor signaling is necessary for microglia viability, unmasking a microglia progenitor cell in the adult brain. *Neuron* 2014;**82**:380−97.

69. Hara T, Chanoch R, Myskiw C, Bussema L, Greenwald A, Kinker G, et al. Cancer-immune cell interactions drive transitions to mesenchymal-like states in glioblastoma. *Cancer Cell* 2021;**39**.

70. Zhou S, Gravekamp C, Bermudes D, Liu K. Tumour-targeting bacteria engineered to Fight cancer. *Nat Rev Cancer* 2018;**18**: 727−43.

71. Zhang X, Hu C, Kong CY, Song P, Wu HM, Xu SC, et al. FNDC5 alleviates oxidative stress and cardiomyocyte apoptosis in doxorubicin-induced cardiotoxicity *via* activating AKT. *Cell Death Differ* 2020;**27**:540−55.

72. Heimann DM, Rosenberg SA. Continuous intravenous administration of live genetically modified *Salmonella typhimurium* in patients with metastatic melanoma. *J Immunother* 2003;**26**:179−80.